Microfabricated Air-core Toroidal Inductor In Very High Frequency Power Converters

Lê Thanh, Hoà; Nour, Yasser; Han, Anpan; Jensen, Flemming; Ouyang, Ziwei; Knott, Arnold

Published in:
IEEE Journal of Emerging and Selected Topics in Power Electronics

Link to article, DOI:
10.1109/JESTPE.2018.2798927

Publication date:
2018

Document Version
Peer reviewed version

Microfabricated Air-core Toroidal Inductor In Very High Frequency Power Converters

Hoa Thanh Le, *Student Member, IEEE*, Yasser Nour, *Member, IEEE*, Anpan Han, *Member, IEEE*, Flemming Jensen, Ziwei Ouyang, *Member, IEEE*, and Arnold Knott *Member, IEEE*

***Abstract*— Miniaturization of power supplies is required for future intelligent electronic systems e.g. internet of things devices. Inductors play an essential role, and they are by far the most bulky and expensive components in power supplies. This paper presents a miniaturized microelectromechanical systems (MEMS) inductor and its performance in a very high frequency (VHF) power converter. The MEMS inductor is a silicon-embedded air-core toroidal inductor, and it is constructed with through-silicon vias, suspended copper windings, silicon fixtures, and a silicon support die. The air-core inductors outperform the silicon-core inductors with higher quality factor at higher frequency. This is verified by small-signal measurements. A 20-turn air-core inductor achieved an inductance of 44.6 nH and a quality factor of 13.3 at 33 MHz, while a silicon-core inductor with the same geometry has a quality factor of 9 at 20 MHz. A DC-DC class-E boost converter is designed and implemented using the fabricated MEMS air-core inductor and a high-performance 65 V gallium nitride field effect transistor. The VHF converter achieved a peak efficiency of 78 % at the input voltage of 6.5 V_{DC}. The MEMS inductor can carry 1 A RMS AC current at 33 MHz and delivers 10.5 W to the output.**

***Index Terms*— Microelectromechanical systems, inductor, DC-DC power converters, zero voltage switching, gallium nitride.**

I. Introduction

POWER supplies are essential sub-systems for modern intelligent electronic devices and systems. They are found in customer electronics, light emitting diode (LED) lightings, and internet of things (IoTs) [1]–[3]. Size, weight, life time, and cost are critical for such applications. While most electronic systems have been advanced rapidly with a dramatic decrease in size and cost, power supply technology is lagging behind. Power supplies are still bulky, inefficient, and costly [4]–[6]. Power supply in package (PwrSiP) [5], [6] and power supply on chip (PwrSoC) [5]–[10] are the vision of power supplies with high efficiency, high power density, and low cost.

This project is a part of TinyPower project which is funded by Innovation Fund (No. 67-2014-1). The first two authors contributed equally to this work.

H. T. Le is with National Center for Micro- and Nanofabrication (DTU Danchip) and DTU Electrical Engineering (DTU Electro), Technical University of Denmark (DTU), 2800 Kongens Lyngby, Denmark. (email: hoalet@dtu.dk)

A. Han and F. Jensen are with DTU Danchip (email: anph@dtu.dk, fj@danchip.dtu.dk)

Y. Nour, Z. Ouyang, and A. Knott are with DTU Electro (e-mail: ynour@elektro.dtu.dk, zo@elektro.dtu.dk, akn@elektro.dtu.dk)

Developing integrated power converter requires miniaturization of energy-storing elements and makes them compatible with the processing flow of integrated circuits. Increasing the switching frequency to the very high frequency range (VHF) (30 MHz – 300 MHz) allows the inductance values needed for PwrSoC to drop to tens of nanohenries (nH).

Taking advantages of microelectromechanical systems (MEMS) fabrication technologies, miniaturized silicon-based inductors can be fabricated with high quality factor, high operating frequency, and high inductance thus enabling their usage in power supplies as energy storage elements. There are two categories of microfabricated inductors: magnetic-core and non-magnetic core inductors. Magnetic-core inductors are typically fabricated with magnetic thin films and two-dimensional (2D) windings such as spiral inductor [11], [12] and race track inductor [13]–[16]). Three-dimensional (3D) windings such as solenoid inductor [17], [18], and toroidal inductor [19], [20] are also possible. High inductance density can be achieved with high permeability core materials, but excessive core loss at VHF operating range is still a major challenge.

Air-core inductors are another solution for VHF power supplies. They have the advantage of no core loss and high frequency operation [21]. Previous works reported on air-core inductors including 2D planar inductors [22], [23], on-substrate 3D inductors [24], [25], and substrate-embedded 3D inductors [26], [27]. In many air-core inductors, the silicon substrate fully or partially remained, which causes undesired parasitic capacitance and eddy-current losses. Thus, quality factor and operating frequency are reduced [27]. Therefore, in the ideal air–core inductor design, the entire core must be removed.

Indeed, with the inductance of tens of nH [22], [26], [27], air-core inductors are suitable for VHF converters. Resonant converters allow the utilization of soft switching techniques due to the intrinsic alternating behavior of current, voltage or both by controlling the switches. Soft switching is desired to minimize the switching losses in the semiconductor devices [28]. High-performance gallium nitride field effect transistors (GaN FETs) have shown a great potential for high-voltage, VHF power supplies. GaN FETs have superior gate charge characteristics compared to other semiconductor transistors [29], [30]. The gate charge (Q_G) multiplied by the on-resistance (R_{DS_ON}) figure of merit shows that GaN FETs can be driven easily compared to their silicon counterparts.

A DC-DC resonant converter consists of two stages which include an inverter stage and a rectifier stage. An inverter stage converts the DC input voltage to AC voltage or current, where after a rectifier stage converts AC current or voltage output of the inverter to a DC voltage or current. A common example of a rectifier stage is a class-D current-driven rectifier that was thoroughly studied and presented in [31], [32].

Inverter design is more challenging. Two examples of inverter topologies are class-E and class-D. The advantage of class-E inverter is that only one low side switch is needed to realize a power stage. However, they have a high voltage stress factor across the switch (drain-to-source voltage divided by the input voltage). This voltage stress can be 3.5 to 4 times higher than input supply voltage [33]–[37]. As a result, a high voltage switch with high breakdown voltage is required.

Class-D inverters on the contrary utilize two switches and have lower voltage stress on switches. The voltage stress equals to the input voltage which allows the usage of higher speed, lower voltage devices [36], [38]. To control two switches, precise design of the gate driver circuitry is needed to avoid cross conduction through the switches which may cause catastrophic failure. Other inverter topologies involve extra circuit components to solve the problem of high voltage stress on the switches [34], [36].

In this paper, a new silicon-embedded air-core toroidal inductor is presented. It has minimal parasitic capacitance and no substrate eddy-current losses due to a complete removal of silicon core. The miniaturized inductor is fabricated by an advanced 3D MEMS fabrication process, characterized by small-signal measurement, and demonstrated in a resonant power converter. The resonant boost converter is based on an agile Schottky-diode based class-D current-driven rectifier and a class-E inverter. The MEMS inductor is used in the resonant network, and a 65 V GaN FET is used as a switch. The converter is optimized to operate in zero voltage switching (ZVS) mode for minimal switching losses. Large signal high-frequency performance of the fabricated inductor is tested in terms of electrical and thermal performance, and AC current capability.

The paper is organized as follows. Section II presents the design and fabrication of the silicon-embedded air-core toroidal MEMS inductor. Section III describes small signal characterization of the MEMS inductor. IV presents design and simulation of a class-E boost converter. Converter performance is presented in Section V, and conclusions follow in Section VI.

II. Inductor Design and Fabrication

A. Inductor Design

The proposed design of a MEMS air-core toroidal inductor is shown in Fig. 1. It is constructed with copper-filled through silicon vias (TSVs), suspended top and bottom windings, five silicon fixtures, and a silicon support die. The TSVs are positioned accordingly to toroidal shape with one TSV at the inner ring and two parallel TSVs at the outer ring. The number of fixtures is selected for mechanical stability of the suspended

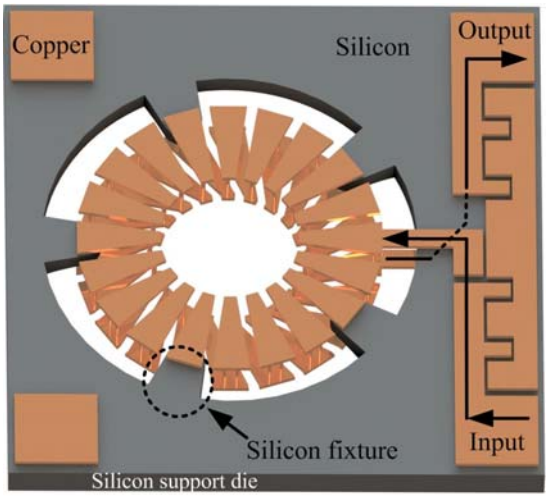

Fig. 1. 3D design of the MEMS air-core toroidal inductor with important features: copper-filled through-silicon vias (TSVs), suspending windings, silicon fixtures, silicon support die, pads for measurement and packaging, and ground-signal-ground probes for wafer-level characterization. The direction of inductor current is depicted by the arrows.

windings. The copper windings are attached to the silicon support die by silicon fixtures that cover outer TSVs and secure the suspended windings. The layout of input and output terminals includes ground-signal-ground pads for on-wafer measurement and two 800 µm x 800 µm pads for connecting to PCB by wire bonding or flip-chip bonding. The direction of current flow is illustrated by the arrows in Fig. 1. The current flows from the input terminal through the windings, comes back to wafer backside, and gets out to the output terminal via through-silicon interconnects as shown by the arrows in Fig. 1.

This air-core design has four main advantages: low parasitic for high Q at high frequency, no substrate eddy-current losses due to a complete removal of silicon core, low electromagnetic interference (EMI) by using self-contained magnetic flux within the toroidal structure, and high compactness with the silicon-embedded construction.

B. Fabrication Technology

The MEMS inductor is fabricated by a novel 3D fabrication process. The process is developed based on MEMS fabrication technologies with the focus on complementary metal oxide semiconductor (CMOS) compatibility, scalability, and flexibility. The inductors can be fabricated with a wide range of geometry and sizes. The process consists of 12 steps and 4 photomasks. The details of fabrication process can be found in our fabrication paper [39]. In this paper, the fabrication process is summarized in four steps (Fig. 2a) as follows.

First, the TSVs are created by deep reactive ion etching (DRIE) (Fig. 2a). A 350-µm-thick silicon wafer is etched through with holes (50 µm diameter) and narrow fixture trenches (3 µm and 7 µm width) which are defined by photolithography. The holes are etched through, while the trenches are not. By the end of step 1, hollow silicon TSVs are created. Second, copper is deposited as the conductive material (Fig. 2b). After depositing insulation layers including aluminum oxide (Al_2O_3) and silicon dioxide (SiO_2), copper is electroplated into the TSVs and on both wafer sides. The

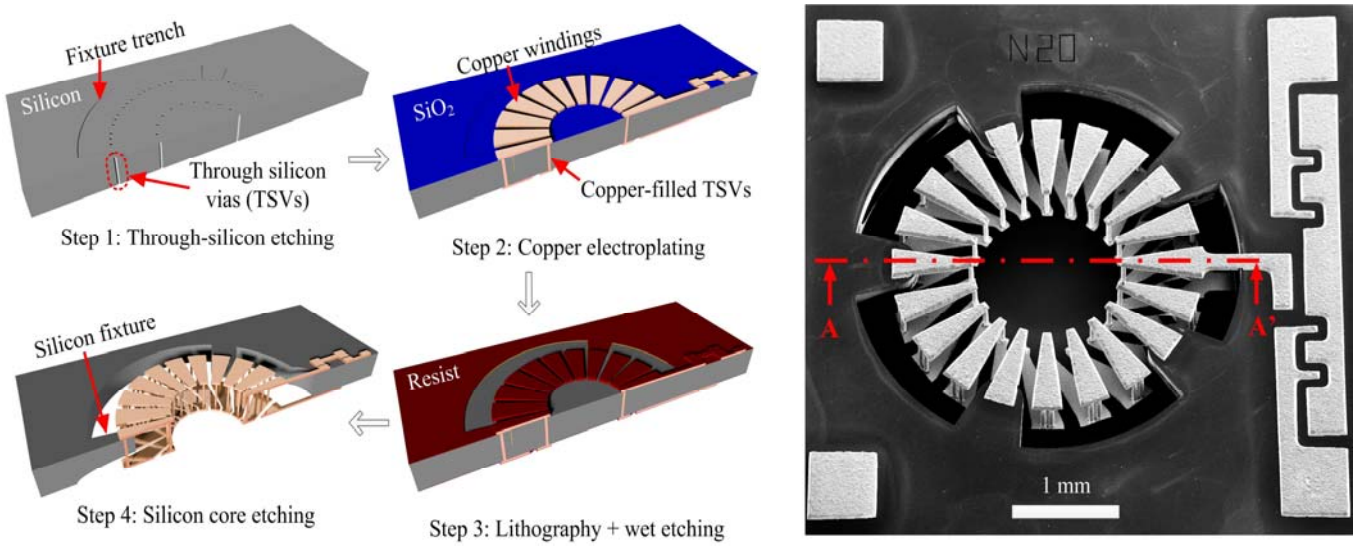

Fig. 2. (a) A four-step fabrication process of MEMS air-core toroidal inductor viewed from direction A-A'. Step 1 is to create 50-µm-diameter through-silicon vias (TSVs) in a 350-µm-thick wafer by deep reactive ion etching and atomic layer deposition. Step 2 includes deposition of insulation layers 50 nm aluminum oxide (Al2O3) and 1.5 µm silicon dioxide (SiO2), electroplating of copper in TSVs and top and bottom conductors, and copper wet etching to define the toroidal windings. Step 3 starts with protecting copper windings by aluminum oxide followed by photolithography of spray-coated resist and wet etching using hydrofluoric acid. Step 4 is to etch the silicon core using dry ICP etching and release the suspended windings by wet etching and drying steps. (b) A secondary electron microscopy (SEM) micrograph of MEMS air-core inductor with 1.5 mm outer diameter, 0.75 mm inner diameter, 20 turns, 350 µm height, and 50 µm TSV diameter. The thickness of top and bottom windings is 50 µm. Winding gap is 94 µm.

aluminum oxide (Al_2O_3) is deposited by atomic layer deposition (ALD) using a process developed for depositing Al_2O_3 on high-aspect-ratio structures [40]. Third, an etching mask is created prior to removal of the silicon core. A 50 nm layer of ALD Al_2O_3 is deposited. Photoresist (AZ 4562, Microchem., USA) is then spray-coated followed by photolithography. It is crucial for the resist to fill and seal the fixture trenches prior to the next Al_2O_3 wet etching step using buffered hydrofluoric acid (BHF). Last, the silicon core is removed using isotropic dry etching by an inductively coupled plasma (ICP) silicon etching tool followed by releasing steps including BHF wet etching, deionized water rinsing, and nitrogen drying. By utilizing Al_2O_3 deposited on the fixture trenches as an etch stop, the silicon core can be removed completely without damaging silicon fixtures. The fixture trenches define the silicon fixtures and support die, thus defining the toroidal core. The process temperature is kept below 200 °C, and this enables post MEMS processing on CMOS wafers and avoid damaging the existing active electronics.

The fabricated MEMS air-core toroidal inductor is shown in Fig. 2. It has 20 turns, 350-µm-tall, and the footprint is 9 mm^2. The silicon core was removed completely while the silicon fixtures and support die remained undamaged. No winding deformation was observed after the releasing steps.

The fabrication process has the advantages of fabricating inductors with a wide range of sizes and shapes. A process yield of 95% was achieved. Magnetic composite core inductors can also be made using the fabricated TSV air-core inductors and a simple screen-printing process. One limitation of the process is a large winding gap of 94 µm due to the Cu wet-etching step. This can be improved by a minor modification in step 2 of the process. For example photoresist is used as a mold for electroplating of Cu.

The thermal and mechanical stability of the fabricated inductors were tested with a thermal cycling test (250 cycles, -45 to 155 °C) and a drop test up to 2 m, respectively. The results are also presented in our fabrication paper [39]. The inductors with the turn/fixture ratio from 6 (30 turns:5 fixtures) to 10 (30 turns:3 fixtures) were tested. They showed good stability after the tests. The suspended windings did not deform and the inductors were still functional. If a higher robustness is required, the air core inductor can be filled with epoxy for stability enhancement.

III. Small Signal Characterization of Inductor

Air-core and silicon-core MEMS inductors were electrically characterized from 0.9 to 110 MHz using a precision impedance analyzer (Agilent 4294A). A dedicated PCB (Fig. 3a) is used as the interface to test the MEMS inductors. An inductor is mounted on the test board using epoxy which is cured at 220 °C for 30 minutes using a convection oven. The inductor input and output terminals are connected to the test board through three 30-µm-diameter gold wires. Impedance analyzer calibration is done with short connection, open connection, and 50 Ω. The calibration boards are shown in Fig. 3b. Short connection is made by three parallel gold wires. Inductance (L), quality factor (Q), and AC resistance (R_{AC}) are measured (Fig. 3c, d).

The air-core inductor has an inductance of 44.6 nH, Q_{peak} of 13.3 at 33.2 MHz. The silicon-core (ρ = 1 - 20 Ωcm) inductor has an inductance of 43.7 nH and lower Q_{peak} of 9 at lower frequency of 20 MHz. The optimal operating frequency of the air-core inductor to be used in the converter is at 33 MHz. At 33 MHz, the AC resistance (R_{AC}) of the air-core inductor is 0.65 Ω which is two times lower compared to 1.25 Ω of the

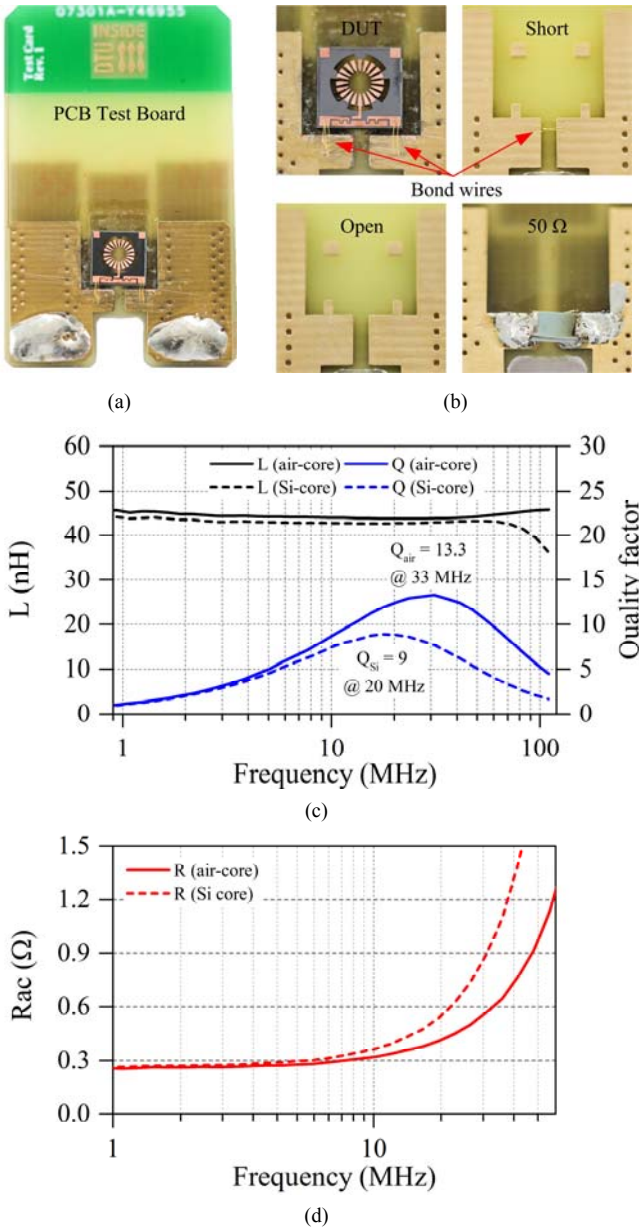

Fig. 3. Small signal characterization of air-core and silicon-core toroidal inductors. (a) PCB test board. An air-core inductor is glue-mounted and connected to the test board through three parallel gold wires. (b) A device under test (DUT) and calibration structures including short connection, open connection, and 50 Ω. (c) Measured inductance (L) and quality factor (Q) in the frequency range from 0.9 MHz to 110 MHz. (d) Measured AC resistance (R_{AC}) in the frequency range from 0.9 MHz to 50 MHz. Air-core and silicon-core inductors have inductance of 44.6 nH and 43.7 nH. Air-core inductor is better than silicon-core inductor with higher Q_{peak} of 13.3 at higher frequency of 33 MHz.

silicon-core inductor. The increase in resistance results in a lower Q factor in the Si-core inductors. This is due to a higher parasitic capacitance and the substrate eddy-current loss of the Si-core inductor. The measured results showed a three-fold higher parasitic capacitance in the Si-core inductor with 11.5 pF compared to 3.7 pF of the air-core inductor, thus allowing the air-core inductor to operate at higher frequency with higher Q factor. This paper focuses on the characterization and demonstration of the fabricated air-core inductors, and the

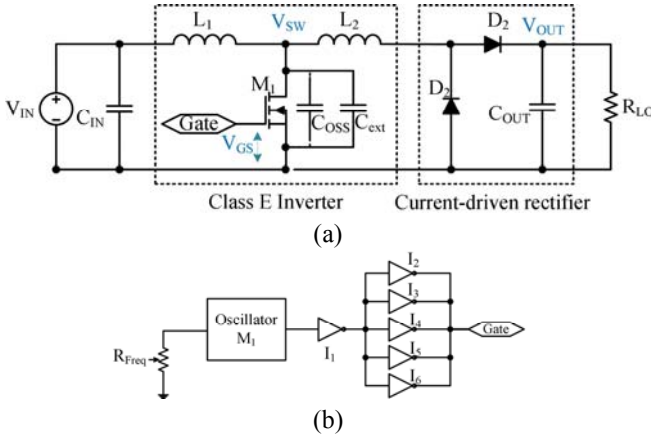

Fig. 4. Circuit diagram of (a) Class E resonant boost converter includes a Class E inverter and a Schottky-diode based class D current driven rectifier. The converter is optimized for zero voltage switching at 33 MHz. (b) frequency-tunable gate driver using silicon oscillator and variable resistor with fixed 50% duty cycle.

models of the air-core toroidal inductors can be found in [41]–[43].

IV. Class-E Resonant Boost Converter

A. Converter Design

To test the inductor, a class-E resonant boost converter has been selected. The converter is designed to operate in ZVS mode at 33 MHz where the inductor has a maximum Q of 13.3, R_{AC} of 0.65 Ω, and L of 44.6 nH. Fig. 4a shows the topology of the resonant converter. The converter consists of two parts: rectifier and inverter.

The first part is a class-D current driven rectifier [31], [32] which is used to drive the load resistance. The rectifier allows DC power flow through D_2 to the load and AC power flow through rectification act. A similar concept was reported in [28] where a resonant type rectifier was used instead of class-D in this case. A reported resonant rectifier [28] is not used in this converter to reduce the amplitude of high frequency current flowing in the inductor under test. This will prevent extra AC losses in the inductor. It is beneficial to deal with D_1 as a freewheeling diode when L_2 current becomes negative.

The second part is the inverter which consists of an input choke (L_1), a GaN FET (M_1), a capacitor (C_{ext}) and finally the inductor under test (L_2). The GaN FET is driven by a logic buffer with an output stage of five inverters connected in parallel as shown in Fig. 4b. The frequency is set by a silicon oscillator with a fixed duty cycle of 50 %. L_2 is used as a part of the resonant network, and it also delivers DC current to the load. L_1 has a high inductance and it is mainly carrying DC current so, the AC losses are minimal.

The working principle of the proposed converter is described by analyzing the steady-state waveforms of switching node voltage (V_{SW}), gate voltage (V_{GS}), and inductor under test current (I_{L2}). It is assumed that the converter perfectly operates in ZVS mode, i.e. the charge stored in the equivalent output capacitance (C_{eqv}) of M_1 is fully discharged before the FET turns on. One switching cycle can be divided into five-time sub-intervals or states as

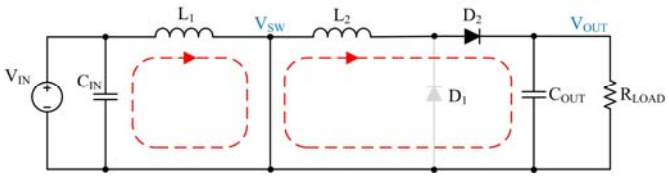

(a) State 1: M_1 ON, D_1 OFF, D_2 ON

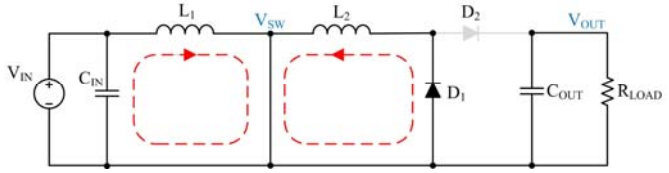

(b) State 2: M_1 ON, D_1 ON, D_2 OFF

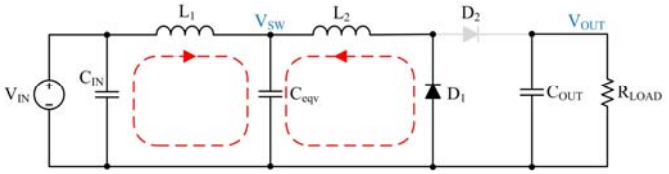

(c) State 3: M_1 OFF, D_1 ON, D_2 OFF

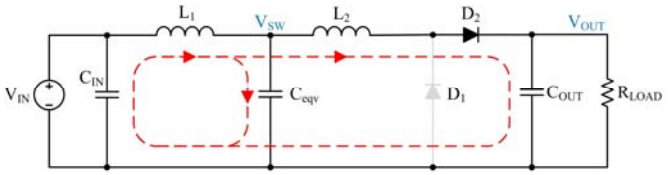

(d) State 4: M_1 OFF, D_1 OFF, D_2 ON

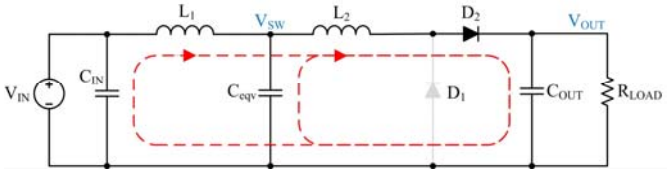

(e) State 5: M_1 OFF, D_1 OFF, D_2 ON

Fig. 5. Working principle of a Class E resonant boost converter is described by analyzing five states of GaN FET (M_1), Schottky diodes D_1, and D_2 corresponding to five time intervals of one switching cycle.as shown ¨' in Fig. 6. The fade color represents the off state of the device.

illustrated in Fig. 5 and Fig. 6.

State 1: the GaN FET M_1 is turned on by the gate driver. L_1 is charged linearly from V_{IN}. L_2 is discharges through D_2 and delivers energy to the load until $I_{L2} = 0$. In ideal operation condition, it is required to switch M1 on when the drain to source voltage is 0 V to achieve soft switching.

State 2: the equivalent capacitance of D_1 is discharged through L_2. I_{L2} changes direction making D_2 reverse biased and D_1 forward biased. L_1 is still being charged by V_{IN}. During this interval, the current flowing in the GaN FET M1 is the summation of I_{L1} and I_{L2} Fig. 5.

State 3: M_1 is turned off by the gate driver. L_2 continue

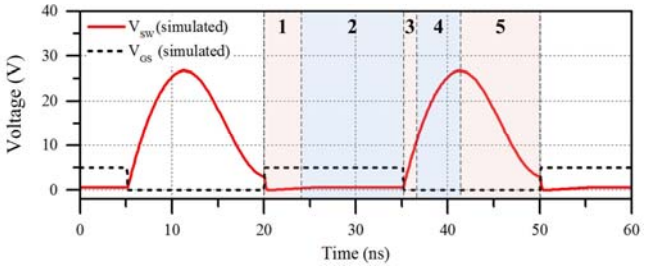

(a)

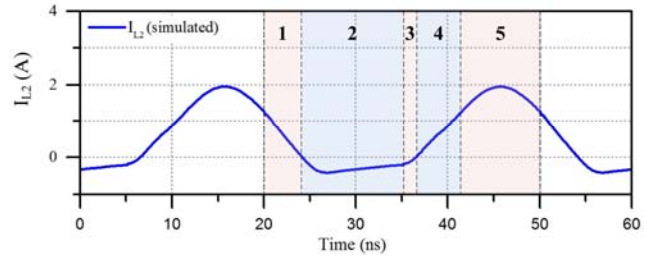

(b)

Fig. 6. Simulated waveforms of (a) Voltage at switching node (V_{SW}) and gate voltage (V_{GS}), (b) inductor under test current (I_{L2}) as function of time from 0 to 60 ns i.e. 2 switching cycles at 33 MHz. A fixed load is set to be 20 Ω. One cycle is divided into five time intervals corresponding to five operation states of M_1, D_1, and D_2.

discharging through D_1 and charging the equivalent output capacitance for the GaN FET (C_{eqv}). C_{eqv} is a combination of the GaN FET output capacitance and an external ceramic capacitor in the circuit (C_{ext}). As a result, the switching node voltage (V_{SW}) is rising. By the end of interval 3, L_2 is fully discharged ($I_{L2} = 0$) and I_{L1} reaches its peak current.

State 4: D_2 is forward biased while D_1 is reverse biased. A part of the stored charge in L_1 is used to charge C_{eqv} so, V_{SW} keeps increasing. Some energy is also transferred to the load through L_2 which is charging in the same time. By the end of interval 4, C_{eqv} is fully charged and V_{SW} reaches a maximum voltage.

State 5: D_1 is off and D_2 is forward biased. C_{eqv} starts to discharge and its current combined with I_{L1} flows to the load. L_2 keep charging until I_{L2} reaches its peak value when V_{SW} equals V_{OUT}. L_2 then discharges through D_2 to the load until I_{L2} equals I_{L1} (C_{eqv} is fully discharged).

B. Simulation

The proposed converter topology is simulated in LT-Spice. The input voltage (V_{IN}) is set to be 8.4 V_{DC} with a fixed 20 Ω load. The simulated waveforms of the switching node (V_{SW}), GaN FET gate-to-source voltage (V_{GS}), and the inductor current (I_{L2}) are shown in Fig. 6. The switching frequency was chosen to be 33 MHz to match the peak quality factor of the MEMS air-core inductor. V_{SW} waveform indicates that the converter is operating close to ZVS mode. C_{eqv} is tuned externally to achieve ZVS operation since L_2 is fixed at 45 nH. A 180-pF external capacitor (C_{ext}) was optimized to achieve soft switching operation at 33 MHz. The choke inductor L_1 is set to a high inductance value as it is assumed to carry DC current with a small AC ripple. L_1 is chosen to be 1 µH. From the waveform of I_{L2}, the root mean square (RMS) inductor current is around 1 A with an average of 0.56 A DC. The

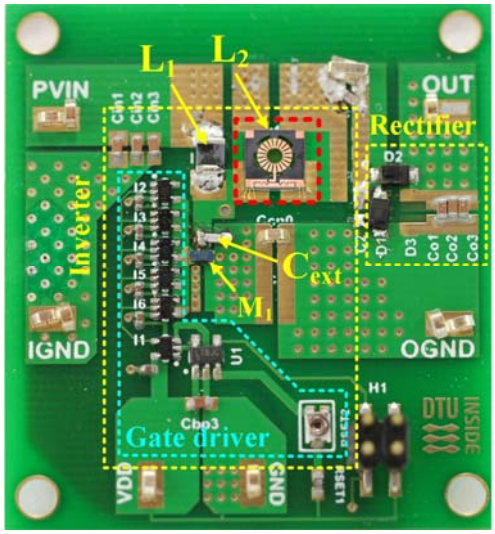

(a)

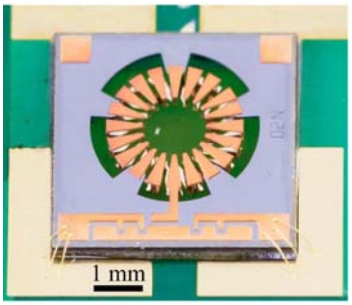

(b)

Fig. 7. (a) Optical image of the converter. (b) A close-up images of an air-core toroidal inductor which is mounted onto PCB by cured epoxy glue. Electrical connections are made by three 30-µm-diameter gold wires bonded in parallel.

simulated voltage conversion ratio (V_{OUT}/V_{IN}) is 1.56.

V. Experimental Results and Discussions

The proposed converter is implemented on a 4 cm x 4 cm PCB (Fig. 7). There are two main blocks corresponding to an inverter and a rectifier (Fig. 7a). A gate driver with tunable silicon oscillator is in the first inverter block. The gate driver is powered by a 5 V external voltage source. Based on simulation results, all components are selected as presented in Table I. A MEMS air-core inductor is mounted using epoxy and connected to the PCB using gold wire bonding. A magnified view of L_2 is shown in Fig. 7b. Here, the integration of L_2 is the prime interest because it is used as an energy-storage element in the resonant network. L_2 carries a high-frequency AC current, it is therefore challenging to integrate due to the excess core loss. On the other hand, L_1 is a 1-µH choke inductor that is used to block the AC current and only carries DC current. The integration of such inductors is less challenging because the unwanted high-frequency effects e.g. eddy currents, core loss, and EMI are not crucial. This allows the use of low-frequency, high-permeability magnetic materials e.g. permalloy (NiFe) and supemalloy (NiFeMo).

The measurement results are shown in Fig. 8 with the measured waveforms of gate and drain voltages. A close operation to ZVS can be observed in Fig. 8 from the

TABLE I
Component Selection

Symbol	Part number	Description
L_2	-	44.6 nH, air-core toroidal inductor
M_1	EPC8002	65 V GaN FET
L_1	LQM32PN1R0MG0L	1 µH, 1.8 A, Multilayer inductor
D_1, D_2	PMEG4010BEA	40 V, 1A, Schottky diode
C_{IN}	GRT188R61H225KE13D	2.2 µF, 50 V, X5R (quantity = 3)
C_{OUT}	GRT188R61H225KE13D	2.2 µF, 50 V, X5R (quantity = 3)
I<1:6>	74LVC1GU04GW-Q100H	Logic inverter chip (quantity = 6)
M1	LTC6905CS5	Tunable silicon oscillator
C_{ext}	GRM1885C1H181JA01D	180 pF ceramic capacitor

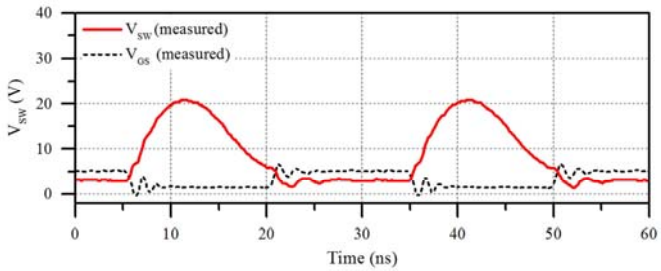

Fig. 8. Measured waveforms. (a) Voltage at switching node (V_{SW}), (b) Gate voltage (V_{GS}).

waveform of V_{SW} when V_{SW} returns to zero before M_1 is turning on. Fig. 9 shows the measured efficiency (η), power loss (P_{LOSS}), output voltage (V_{OUT}), and output power (P_{OUT}) of the converter with a sweep of input voltage (V_{IN}) from 3 V to 10 V. The average conversion ratio (V_{OUT}/V_{IN}) is 1.48. The efficiency without gate driver loss (η_{WO_GD}) increases from 73.4 % to 77.3 % with V_{IN} from 3 V to 10 V, and then saturates with an efficiency of about 77 %. The converter achieved a peak efficiency of 77.3 % at an input voltage V_{IN} = 6.5 V with an output voltage of V_{OUT} 9.7 V and an output power level of P_{OUT} = 6.1 W. The total power loss P_D is 1.5 W. The converter can delivery up to 14.5 V V_{OUT} and 10.5 W P_{OUT}. At the target switching frequency of 33 MHz, the gate driver loss is 0.15 W. The efficiency including the gate driver loss and the oscillator (η_{W_GD}) is 75.5%. For testing purposes, the gate driver is built externally, but the gate driver loss can be reduced by proper design of the gate driver with an integrated circuit process.

The MEMS inductor AC power loss was estimated via DC power loss using thermal measurement method. The idea is to drive an increasing DC current through the inductor until its thermal image is matched with its thermal image during AC converter operation. The DC power loss is obtained by multiplying the inductor voltage by the applied DC current. Fig. 10b and c show a matching of inductor temperature for the AC and DC power loss, respectively. A DC current of 1.53 A was measured with a 0.646 V DC voltage. The DC power loss is then calculated to be 0.98 W which equals to the AC power loss. In addition, the high-temperature DC resistance of the inductor is measured to be 0.42 Ω.

Fig. 10 shows thermal images of the converter with 8.4 V V_{IN}. The GaN FET temperature is 77.4 °C. Because of Cu reflects in the thermal image, an absolute thermal measurement of Cu is not possible, and the copper windings

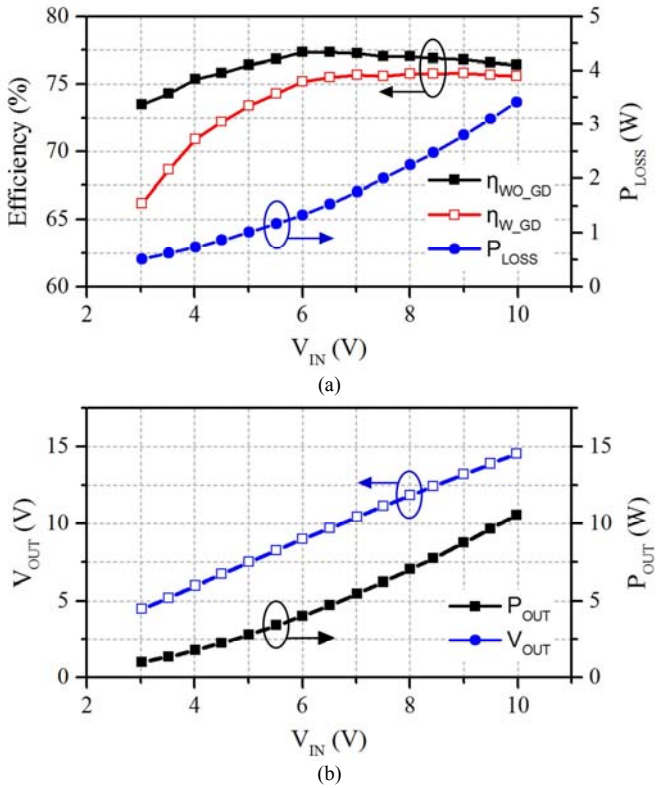

Fig. 9. Characterization results of boost converter using a microfabricated air-core inductor. (a) Efficiency of the converter without loss in gate driver (η_{WO_GD}), with loss in gate driver (η_{WO_GD}), and total power loss (P_{LOSS}) including gate driver loss of 0.15 W versus input voltage (V_{IN}). (b) Output power (P_{OUT}) and output voltage (V_{OUT}) versus V_{IN}.

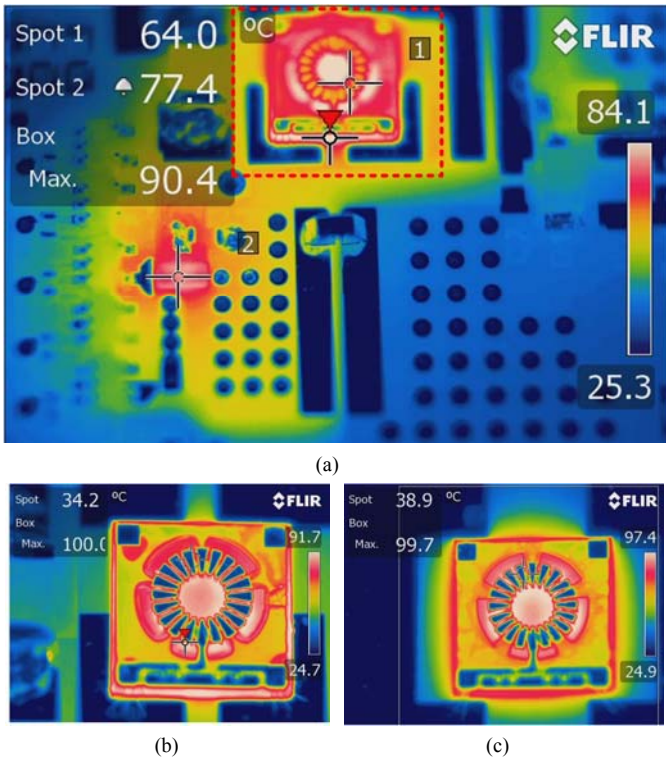

Fig. 10. (a) Thermal images of converter with V_{IN} = 8.4 V captured by FLIR camera T600 (FLIR, USA) using standard lens. Close-up thermal images of the microfabricated inductor for two cases: (b) large signal performance with AC current from the converter and (c) DC current testing with an equivalent thermal performance. DC power loss in the inductor is 0.98 W with 1.53 A DC current and 0.646 V. The close-up images were captured by a FLIR close-up IR 2.9x lens with 50 µm detector pitch. The measurement condition is with air-flow and without thermal pad for cooling down underneath the die. There is signal reflected from the board which induces biases to the measured temperature.

temperature can be estimated by matching the measured DC resistance at room temperature to the DC resistance measured at high temperature. The details of DC resistance measurement at room temperature and the method to estimate the absolute Cu temperature are presented in the Appendix. The temperature of the copper windings is calculated to 108 °C which is slightly above the temperature of the silicon die in Fig. 10b. The thermal performance of the air-core inductor can be improved by implementing a thermal pad underneath the inductor.

For better performance, the toroidal windings can be further optimized to achieve a lower resistance and a higher inductance density which will result in smaller inductors. The improvements can be made on the TSV design, e.g. increasing the diameter and the density of the circular TSVs will result in a lower resistance. Alternatively, using a single rectangular outer TSV will also increase winding coverage and lead to a lower resistance. Parallel inner TSVs will have a significant improvement in the resistance, but the effective toroidal-core volume will reduce. This can be done with a two-step deep reactive ion etching (DRIE) and electrodeposition process. A simple process modification can increase the winding thickness and density: using mold-based electrodeposition as a replacement for copper wet-etching. Mold-base technology was reported in [44] for a racetrack inductor, which has a copper thickness of 85 µm and a winding gap of 5 µm.

The heat-dissipation performance of the air-core and Si-core inductors was compared in our fabrication paper [39]. The efficiency is 64 % with the Si-core inductor and 68% with the air-core inductor with 30 °C higher than that of the air-core inductor. Indeed, the Si core has a much higher thermal conductivity for heat dissipation, but with the same windings, the air-core inductor has lower resistance compared to that of the Si-core due to: capacitive coupling and the eddy-current loss in the Si substrate. At 33 MHz, the Si-core inductor has a resistance of 1.25 Ω compared to 0.65 Ω of the air-core inductor. To further improve heat dissipation, the MEMS air-core inductor can be filled with thermal epoxy, which has a better thermal conductivity and extremely high resistivity. E.g. EPO-TEK® 921-FL (Epotek, USA) which has k = 1.1 W/mK, and $\rho > 6.\ 10^{13}$ Ωcm. We developed a screen-printing process and demonstrated an implementation of a magnetic composite core using epoxy and NiZn powders [45]. This process can also be used for making a thermal-epoxy core inductor.

VI. Conclusion

A study on silicon-embedded air-core toroidal MEMS inductor for PwrSoC applications has been presented. The proposed microfabrication process enables fabrication of 3D MEMS toroidal inductor with a unique air-core design. The inductors are embedded in a silicon substrate with through-

silicon vias and suspended copper windings. The silicon-core has been removed completely to increase the quality factor and operating frequency. Air-core and silicon-core inductors were electrically characterized and compared. The results imply that the air-core inductors are better for very high frequency operation with higher quality factor at higher frequency. The MEMS air-core inductor has a quality factor of 13.3 at 33 MHz while a silicon-core inductor has a quality factor of 9 at 20 MHz. A VHF class-E boost converter was designed and optimized for zero voltage switching using the MEMS inductor and a GaN FET. The testing results showed that the inductor can handle an RMS current of 1 A and deliver a maximum power of 10.5 W to the output with a peak efficiency of 77.3 %. Based on our results that laid the cornerstone of MEMS inductor applications in power converters, we believe that MEMS inductors will play an important role for the development and realization of the PwrSoC vision.

APPENDIX

The absolute temperature of the copper windings (T) can be estimated by a linear approximation (1) [46].

$$T = \frac{R_T/R_0 - 1}{\alpha_{Cu}} + T_0 \qquad (1)$$

where α_{Cu} = 4.29 (ppm/K) is the temperature coefficient of copper. T_0 is room temperature of 22 °C. R_T is the DC resistance measured at T °C which equals to 0.42 Ω. R_0 is the DC resistance measured at room temperature. R_0 At room temperature, the DC resistance (R_0) is re-measured precisely by applying a small DC current and measure the voltage across the inductor. An average R_0 of 0.308 Ω is measured including gold wires and PCB parasitic. The details of DC resistance measurement are presented in Table II. The absolute temperature of the copper windings (T) is calculated to be 108 °C.

TABLE II
MEASUREMENT OF DC RESISTANCE INCLUDING GOLD WIRES AND PCB PARASITICS AT ROOM TEMPERATURE

Applied DC current (mA)	Measured voltage (mV)	DC Resistance (Ω)
10.37	3.2	0.309
20.33	6.24	0.307
30.5	9.38	0.308
40.45	12.43	0.307
50.36	15.48	0.307
100.67	31.03	0.308
200.66	62.09	0.309
	Average	0.308

ACKNOWLEDGEMENT

This work has been conducted in National Center for Micro- and Nanofabrication (DTU Danchip) and DTU Electrical Engineering. This project is a part of TinyPower project which is funded by Innovation Fund (No. 67-2014-1).

REFERENCES

[1] D. Bandyopadhyay and J. Sen, "Internet of things: Applications and challenges in technology and standardization," in *Wirel. Pers. Commun.*, 2011, vol. 58, no. 1, pp. 49–69.

[2] D. Miorandi, S. Sicari, F. De Pellegrini, and I. Chlamtac, "Internet of things: Vision, applications and research challenges," *Ad Hoc Networks*, vol. 10, no. 7. pp. 1497–1516, 2012.

[3] S. Li, L. Da Xu, and S. Zhao, "The internet of things: a survey," *Inf. Syst. Front.*, vol. 17, no. 2, pp. 243–259, 2015.

[4] G. Sauerländer, D. Hente, H. Radermacher, E. Waffenschmidt, and J. Jacobs, "Driver electronics for LEDs," in *Conf. Rec. IEEE 41st IAS Annu. Meet.*, 2006, vol. 5, pp. 2621–2626.

[5] S. C. O'Mathuna, "PwrSiP power supply in package power system in package," in *2016 Int. Symp. 3D Power Electron. Integr. Manuf.*, 2016, pp. 1–21.

[6] F. Waldron, R. Foley, J. Slowey, A. N. Alderman, B. C. Narveson, and S. C. Ó Mathúna, "Technology roadmapping for power supply in package (PSiP) and power supply on chip (PwrSoC)," *IEEE Trans. Power Electron.*, vol. 28, no. 9, pp. 4137–4145, 2013.

[7] M. Araghchini *et al.*, "A Technology Overview of the PowerChip Development Program," *IEEE Trans. Power Electron.*, vol. 28, no. 9, pp. 4182–4201, 2013.

[8] S. C. Ó. Mathúna, T. O'Donnell, N. Wang, and K. Rinne, "Magnetics on silicon: An enabling technology for power supply on chip," *IEEE Trans. Power Electron.*, vol. 20, no. 3, pp. 585–592, 2005.

[9] C. Ó. Mathúna, N. Wang, S. Kulkarni, and S. Roy, "Review of integrated magnetics for Power Supply on Chip (PwrSoC)," *IEEE Trans. Power Electron.*, vol. 27, no. 11, pp. 4799–4816, 2012.

[10] D. Disney and Z. J. Shen, "Review of silicon power semiconductor technologies for power supply on chip and power supply in package applications," *IEEE Trans. Power Electron.*, vol. 28, no. 9, pp. 4168–4181, 2013.

[11] E. J. Brandon, E. Wesseling, V. White, C. Ramsey, L. Del Castillo, and U. Lieneweg, "Fabrication and characterization of microinductors for distributed power converters," *IEEE Trans. Magn.*, vol. 39, no. 4 II, pp. 2049–2056, 2003.

[12] J. Li, V. Tseng, Z. Xiao, and H. Xie, "A High-Q In-Silicon Power Inductor Designed for Wafer-Level Integration of Compact DC-DC Converters," *IEEE Trans. Power Electron.*, vol. 32, no. 5, pp. 1–1, 2016.

[13] C. R. Sullivan and S. R. Sanders, "Design of microfabricated transformers and inductors for high-frequency power conversion," *IEEE Trans. Power Electron.*, vol. 11, pp. 228–238, 1996.

[14] N. Wang, T. O'Donnell, S. Roy, P. McCloskey, and C. O'Mathuna, "Micro-inductors integrated on silicon for power supply on chip," *J. Magn. Magn. Mater.*, vol. 316, no. 2 SPEC. ISS., pp. e233–e237, Sep. 2007.

[15] T. Liakopoulos, A. Panda, M. Wilkowski, and A. Lotfi, "Manufacturing Development of a New Electroplated Magnetic Alloy Enabling Commercialization of PwrSoC Products," in *Int. Work. Power Supply Chip*, 2012.

[16] N. Sturcken *et al.*, "A 2.5D integrated voltage regulator using coupled-magnetic-core inductors on silicon interposer," *IEEE J. Solid-State Circuits*, vol. 48, no. 1, pp. 244–254, 2013.

[17] S. X. Wang, "Fabrication and Analysis of High-Performance Integrated Solenoid Inductor With Magnetic Core," *IEEE Trans. Magn.*, vol. 44, no. 11, pp. 4089–4095, Nov. 2008.

[18] D. Dinulovic, M. Haug, J. Thone, and M. C. Wurz, "Microtransformer / Microinductor on Silicon for Point-of-Load High Frequency Power Applications," *Int. Work. Power Supply Chip*, 2016.

[19] A. Camarda, E. Macrelli, M. Tartagni, R. P. Paganelli, and A. Romani, "Design and Fabrication of Bond Wire Micro-Magnetics with LTCC core," in *Int. Work. Power Supply Chip*, 2016, pp. 1–38.

[20] J. Kim, J.-K. Kim, M. Kim, F. Herrault, and M. G. Allen, "Microfabrication of toroidal inductors integrated with nanolaminated ferromagnetic metallic cores," *J. Micromech. Microeng.*, vol. 23, no. 11, p. 114006, Nov. 2013.

[21] R. Meere, T. O'Donnell, S. Kulkarni, S. Roy, and S. C. O'Mathuna, "Magnetic-Core and Air-Core Inductors on Silicon: A Performance Comparison up to 100 MHz," *IEEE Trans. Magn.*, vol. 47, no. 10, pp. 4429–4432, Oct. 2011.

[22] C. D. Meyer, S. S. Bedair, B. C. Morgan, and D. P. Arnold, "Influence of layer thickness on the performance of stacked thick-film copper air-core power inductors," *IEEE Trans. Magn.*, vol. 48, no. 11, pp. 4436–4439, 2012.

[23] J. Y. Park and M. G. Allen, "High Q spiral-type microinductors on silicon substrates," *IEEE Trans. Magn.*, vol. 35, no. 5 PART 2, pp. 3544–3546, 1999.

[24] J. Kim, F. Herrault, X. Yu, M. Kim, R. H. Shafer, and M. G. Allen, "Microfabrication of air core power inductors with metal-encapsulated polymer vias," *J. Micromech. Microeng.*, vol. 23, no. 3, p. 35006, Mar. 2013.

[25] U. Schürmann *et al.*, "Fabrication of toroidal microinductors for RF applications," in *IEEE Trans. Magn.*, 2009, vol. 45, no. 10, pp. 4770–4772.

[26] L. Gu and X. Li, "High-Q solenoid inductors with a CMOS-compatible concave-suspending MEMS process," *J. Microelectromechanical Syst.*, vol. 16, no. 5, pp. 1162–1172, 2007.

[27] X. Yu, M. Kim, F. Herrault, C.-H. Ji, J. Kim, and M. G. Allen, "Silicon-Embedding Approaches to 3-D Toroidal Inductor Fabrication," *J. Microelectromechanical Syst.*, vol. 22, no. 3, pp. 580–588, Jun. 2013.

[28] J. M. Burkhart, R. Korsunsky, and D. J. Perreault, "Design Methodology for a Very High Frequency Resonant Boost Converter," *IEEE Trans. Power Electron.*, vol. 28, no. 4, pp. 1902–1909, 2010.

[29] Y. Nour, Z. Ouyang, A. Knott, and I. H. H. Jørgensen, "Design and Implementation of High Frequency Buck Converter Using Multi-Layer PCB Inductor," *42nd Annu. Conf. IEEE Ind. Electron. Soc.*, pp. 1313–1317, 2016.

[30] Y. Nour, A. Knott, and I. H. H. Jørgensen, "Investigating Enhancement Mode Gallium Nitride Power FETs in High Voltage , High Frequency Soft Switching Converters," in *Int. Conf. Power Electron. Mach. Drives*, 2016, pp. 1–5.

[31] M. K. Kazimierczuk, "Class D Current-Driven Rectifiers for Resonant DC/DC Converter Applications," *IEEE Trans. Ind. Electron.*, vol. 38, no. 5, pp. 344–354, 1991.

[32] M. K. Kazimierczuk and D. Czarkowski, *Resonant Power Converters*, vol. 7, no. June. 2012.

[33] K. Peng and E. Santi, "Class E Resonant Inverter Optimized Design for High Frequency (MHz) Operation Using eGaN HEMTs," in *Appl. Power Electron. Conf. Expo.*, 2015, pp. 2469–2473.

[34] J. M. Rivas, Y. Han, O. Leitermann, A. D. Sagneri, and D. J. Perreault, "A high-frequency resonant inverter topology with low-voltage stress," *IEEE Trans. Power Electron.*, vol. 23, no. 4, pp. 1759–1771, 2008.

[35] A. Knott *et al.*, "Evolution of Very High Frequency Power Supplies," *IEEE J. Emerg. Sel. Top. Power Electron.*, vol. 2, no. 3, pp. 386–394, Sep. 2014.

[36] M. Madsen, A. Knott, and M. A. E. Andersen, "Low power very high frequency switch-mode power supply with 50 v input and 5 v output," *IEEE Trans. Power Electron.*, vol. 29, no. 12, pp. 6569–6580, 2014.

[37] J. A. Pedersen, M. P. Madsen, A. Knott, and M. A. E. Andersen, "Self-oscillating Galvanic Isolated Bidirectional Very High Frequency DC-DC Converter," in *Appl. Power Electron. Conf. Expo.*, 2015, pp. 1974–1978.

[38] M. P. Madsen, A. Knott, and M. A. E. Andersen, "Very high frequency half bridge DC/DC converter," *2014 IEEE Appl. Power Electron. Conf. Expo. - APEC 2014*, pp. 1409–1414, 2014.

[39] H. T. Le, I. Mizushima, P. T. Tang, Z. Ouyang, F. Jensen, and A. Han, "Fabrication of 3D Air-core MEMS Inductors for High Frequency Power Electronic Applications," *Microsystems Nanoeng.*, vol. 3, 2017, DOI. 10.1038/micronano.2017.82.

[40] E. Shkondin *et al.*, "Fabrication of high aspect ratio TiO_2 and Al_2O_3 nanogratings by atomic layer deposition," *J. Vac. Sci. Technol. A Vacuum, Surfaces, Film.*, vol. 34, no. 3, p. 31605, 2016.

[41] C. R. Sullivan, S. Prabhakaran, S. Lu, C. R. Sullivan, W. Li, and S. Prabhakaran, "Design and Fabrication of Low-Loss Toroidal Air-Core Inductors," no. June, pp. 1754–1759, 2007.

[42] M. Araghchini *et al.*, "Modeling and Measured Verification of Stored Energy and Loss in MEMS Toroidal Inductors," vol. 50, no. 3, pp. 2029–2038, 2014.

[43] G. Zulauf, W. Liang, and J. Rivas-davila, "A Unified Model for High-Power , Air-Core Toroidal PCB Inductors," in *IEEE Work. Control Model. Power Electron.*, 2017.

[44] R. Anthony, E. Laforge, D. P. Casey, J. F. Rohan, and C. O'Mathuna, "High-aspect-ratio photoresist processing for fabrication of high resolution and thick," *J. Micromech. Microeng.*, vol. 26, no. 10, p. 105012, 2016.

[45] H. T. Le *et al.*, "High-Q 3D Microfabricated Magnetic-core Toroidal Inductors for Power Supplies in Package," *unpublished*.

[46] J. H. Dellinger, "The temperature coefficient of resistance of copper," *J. Franklin Inst.*, vol. 170, no. 3, pp. 213–216, 1910.

Hoa Thanh Le (S'15) received the B.Sc. degree in Electronics and Telecommunications from Ho Chi Minh University of Technology, Vietnam, in 2012 and the M:Sc. degree in Microsystem Engineering from University College of Southeast Norway, Norway, in 2014. He is currently pursuing the PhD degree in Micro and Nanofabrication at Technical University of Denmark. His research interests include micro- and nanofabrication, passive components, and high frequency magnetics.

Yasser Nour (S'07, M'17) received the B.Sc. and M.Sc. degrees in Electrical Engineering from South Valley University, Egypt in 2007 and 2011 respectively. He was a research engineer at Enpirion Inc., a staff engineer at Altera's Egypt Technology Center, and a staff engineer at Symmid Corporation Sdn. Bhd. in Malaysia. He is currently pursuing the PhD in electrical engineering at Technical University of Denmark. His research interests include analog integrated circuits design, integrated power converters, high voltage low power converters, integrated magnetics and passive components.

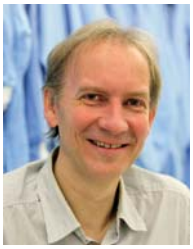

Flemming Jensen received the Ph.D. degree in Physics from the Department of Physics and Astronomy at Aarhus University, Denmark, in 1992. From 1992 until 1997 he worked as a researcher at the newly established cleanroom facility, Microelectronics Center (MIC) – from 2004 renamed DTU Danchip - at the Technical University of Denmark establishing and developing new fabrication technologies in etching and thin film deposition mainly for the silicon based platform. From 1997 he has been an Associate Professor conducting and supporting research projects related to micro- and nanofabrication within various research topics. From 2004 he has been member of the management at DTU Danchip heading the Process Engineering group. In the later years his main focus has been on advanced high density plasma etching techniques for many different material platforms and establishing atomic layer deposition for conformal growth of very thin layers.

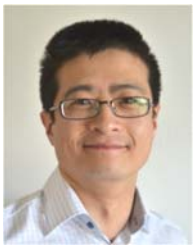

Anpan Han (M' 12) received the B.Sc. and M.Sc. degree in biophysics from the Niels Bohr Institute, University of Copenhagen, Denmark, in 2002. He received the Ph.D. degree in Micro and Nanotechnology from Institute of Microtechnology (now part of EPFL), Université de Neuchâtel, Switzerland in 2006. Currently, he is an assistant professor at Danchip, Technical University of Denmark since 2014. His research is in nanofabrication technology and science, with focus in diamond MEMS, complex MEMS process integration and electron beam lithography.

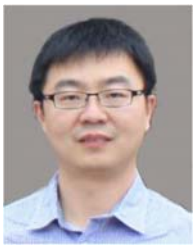

Ziwei Ouyang (S'07, M'11) received the B.S degree in electrical engineering from the Naval University of Engineering, Wuhan, China, in 2004, the M.S degree from the Tianjin University of Technology, Tianjin, China, in 2007, and the Ph.D. degree from the Technical University of Denmark (DTU), Denmark, in 2011. He worked as Postdoctoral Researcher and assistant professor in the Department of Electrical Engineering at DTU from 2011 to 2016 and is currently associate professor in the same department. His research areas focus on high-frequency planar magnetics modeling and integration, high-density high-efficiency power converters, PV battery energy storage system, and wireless charging etc. He has over 50 peer-reviewed journal and conference publications and currently he is the holder of five US/EP/PCT patents. He received the Young Engineer Award at PCIM Asia 2014 and Best Paper Awards in ECCE Asia conferences in 2010 and 2012, respectively. He is an IEEE senior member.

Arnold Knott (M'10) received the Diplom-Ingenieur (FH) degree from the University of Applied Sciences in Deggendorf, Germany, in 2004. From 2004 until 2009 he has been working with Harman/Becker Automotive Systems GmbH in Germany and USA, designing switch-mode audio power amplifiers and power supplies for automotive applications. In 2010 he earned the Ph.D. degree from the Technical University of Denmark, Kongens Lyngby, Denmark working on a research project under the title "Improvement of out-ofband Behaviour in Switch-Mode Amplifiers and Power Supplies by their Modulation Topology". From 2010 to 2013 he was Assistant Professor and since 2013 Associate Professor at the Technical University of Denmark. His interests include switch-mode audio power amplifiers, power supplies, active and passive components, integrated circuit design, acoustics, radio frequency electronics, electromagnetic compatibility and communication systems.